RESEARCH ARTICLE

Statistical approach to design Zn particle size, shape, and crystallinity for alkaline batteries

Brian Lenhart¹, Devadharshini Kathan¹, Valerie Hiemer¹,², Mike Zuraw³, Matt Hull³, William E. Mustain (⋈)¹

Department of Chemical Engineering, University of South Carolina, Columbia, SC 29208, USA
 Department of Chemical Engineering, Virginia Polytechnic Institute, Blacksburg, VA 24060, USA
 Juracell, Bethel, CT 06801, USA

© Higher Education Press 2024

Abstract In modern alkaline batteries, the zinc anode is the performance-limiting and lifetime-limiting electrode, making the choice of zinc powder critical. Due to the various material fabrication processes that are used to manufacture industrial zinc powder, there exists a wide array of possible zinc particle shapes, sizes, and crystallinities. These industrial zinc powders are typically conceived, produced, and tested through trial-and-error processes using historical "rules of thumb." However, a data-driven approach could more effectively elucidate the optimum combination of zinc particle properties. In this paper, the effect of Zn particle size, shape, and crystallinity on the achievable capacity and corrosion current is investigated. The Zn types are tested in both powder and slurry form. Following the data collection, a factorial-based statistical analysis is performed to determine the most statistically significant variables affecting capacity and corrosion. This information is then used to down-select to a subset of particles that are tested in cylindrical cells with an AA-equivalent geometry. The reported technique can be used to develop actionable principles for battery manufacturers to create cells that are more stable, longer lasting, and have higher energy densities.

Keywords zinc, anode, battery, optimization, capacity, corrosion

1 Introduction

Primary alkaline batteries are widely used in many portable electronic devices due to their high energy density, long shelf life, and low cost. Zinc is the preferred anode in these cells due to its high energy density, high earth abundance, high columbic efficiency, as well as its versatility, safety, and environmental friendliness [1-3]. Despite these advantages, there are drawbacks to the zinc anode, such as low operating voltage, corrosion (also known as H₂ gassing, leading to cell rupture and device damage), and passivation (leading to reduced material utilization in primary applications, and limited cycle life in secondary applications) [4–6]. It is well known that the electrode limiting the performance of primary alkaline batteries is the zinc anode, which consists of zinc powder mixed with a gelled alkaline electrolyte producing a stable slurry of well-dispersed zinc particles [7]. Since

the performance of primary alkaline batteries is driven by the corrosion resistance and achievable capacity of the zinc anode, literature has focused on reducing gassing and increasing material utilization, which translates to practical systems as improved shelf life and energy density, both of which are market drivers.

Discharge of zinc slurry anodes in alkaline electrolyte occurs via a 2-stage process. The first step, Eq. (1), is the two-electron oxidation of metallic Zn to zincate, which is soluble in the electrolyte. When the zincate concentration reaches a critical level, dehydration occurs, yielding a ZnO passive film, water, and alkali (Eq. (2)).

$$Zn + 4OH^{-} \rightarrow Zn(OH)_{4}^{2-} + 2e^{-}$$
 (1)

$$Zn(OH)_4^{2-} \rightarrow ZnO + 2H_2O + 2OH^-$$
 (2)

During discharge and storage, zinc particles in the alkaline slurry undergo thermodynamically spontaneous corrosion where Zn reacts electrochemically with water (Eq. (3)) to form the net corrosion products of hydrogen gas and $Zn(OH)_4^{2-}$ (Eq. (4)) [8].

$$2H_2O + 2e^- \rightarrow H_2 + 2OH^-$$
 (3)

$$Zn + H_2O + 2OH^- \rightarrow H_2 + Zn(OH)_4^{2-}$$
 (4)

Left unimpeded, hydrogen accumulation can lead to cell rupture and leakage of caustic electrolyte into electronic devices, causing damage. Because the corrosion process occurs at different rates on each crystal facet of the zinc lattice, it should be feasible to engineer a material that has a high degree of corrosion resistance if certain crystal planes are preferentially oriented [9]. Further, zinc materials have been noted to experience intergranular corrosion, where the electrolyte penetrates and diffuses along grain boundaries and dissolves the zinc from within, causing the particles to become brittle. disintegrate, and overall reduce material utilization [10]. It should also be noted that particle sizes within commercial zinc powder are not uniformly distributed and fall within the typical range of 20–500 µm. Considering that smaller particles within the powder have larger surface area-to-volume ratios than larger particles, and that corrosion happens at the solid-liquid interface, it is expected that particle size can also play a contributing role in corrosion propensity. Additionally, the general morphological shapes of particles have been shown to influence corrosion rates [9,11]. Combined, these observations suggest that a theoretically optimal zinc powder exists where the particle shape, size, and crystallinity of the powder can be carefully engineered to maximally suppress corrosion.

Though suppressing corrosion is important, it alone does not define anode performance. The achievable capacity of zinc is also extremely important. When studying the achievable capacity of zinc, the two most common form factors are zinc foils (academia) and zinc powders (industry) [9,12–15]. Zinc foils are easy to handle and can be good representatives of general electrochemical zinc behavior, but they have a low electrochemically active surface area (ECSA), which leads to a low rate capability and low material utilization [6,16]. Zinc powders, on the other hand, have a high ECSA and can achieve high-rate discharge but are more prone to passivation and corrosion [9,17–21]. Therefore, powders are preferred in practical systems.

Researchers have studied a wide array of non-commercial zinc particle structures in alkaline electrolytes and slurries, including fibrous, mesh, foam, sponge, nanostructured, encapsulated, alloyed (e.g., zinc–aluminum) and composite (e.g., zinc–carbon) [1,22–32]. While many of these more complex zinc anodes perform well at suppressing corrosion, maximizing material utilization for deep discharge primary applications, and/or extending durability and cyclability in secondary applications, unfortunately they are generally not feasibly scaled. Therefore, zinc powders that can be produced economically at scale remain the only reasonable options to consider for commercial applications.

Fortunately, zinc powder manufacturing is well developed and there are several existing processes that can be utilized, including electrodeposition, spray pyrolysis, ball milling, microemulsion, thermal decomposition, laser ablation, polyol synthesis, and chemical and physical vapor deposition [27,28,33-39]. In total, these methods provide a large cache of possible powders with different sizes, shapes, porosities, surface roughnesses, crystallinities, etc. The most common industrially manufactured zinc microparticle shapes are spherical, tubular, flat, and irregular. Mentioned earlier, zinc powders made for modern alkaline batteries have an average particle size ranging from 20 to 500 µm with a wide size distribution (Fig. S1 in Electronic Supplementary Material) [40]. In addition to particle size and shape, the crystallinity (grain size) of zinc particles can vary widely depending on the synthesis method or conditions. Since zinc powders come in a myriad of sizes, shapes, and crystallinities, all of which can contribute to the anode performance, developing a method for systematically screening the electrochemical performance of zinc powder for primary commercial battery applications is highly desirable.

In this paper, zinc particles with four geometric particle shapes (sphere, tube, flat, and irregular), four particle sizes (< 53, 53-106, 106-150, and 150-250 µm), and four particle heat treatments (grain size/crystallinity manipulation) (Fig. 1) were systematically isolated and investigated. These combinations of particle size, shape, and crystallinity were the basis for a 64-powder type, 4^k factorial design of experiments (DOEs) study. Once prepared, each powder was then probed for corrosion and achieved capacity values with an in-house, ex-situ, 3electrode analytical platform, in both powder and slurry forms. A statistical analysis was performed on the measured corrosion current and achieved capacity values to determine the most significant variables driving their behavior. Based on the ex-situ analysis of the powder and slurry anodes, the best performing zinc materials were deployed in in-situ AA-replica cells and compared to a control powder comprised by multiple particle shapes and sizes. This paper demonstrates the power of a systematic DOE coupled with a high throughput 3-electrode electroanalytical platform to facilitate the analysis and improvement of battery active materials for commercial platforms and to reduce the amount of overall test material, time, and personnel needed.

2 Materials and methods

2.1 Powder preparation

Four proprietary zinc powders were selected for study based on their dominant particle shape. The dominant particle shapes were spheres, tubes, flats, and irregular.

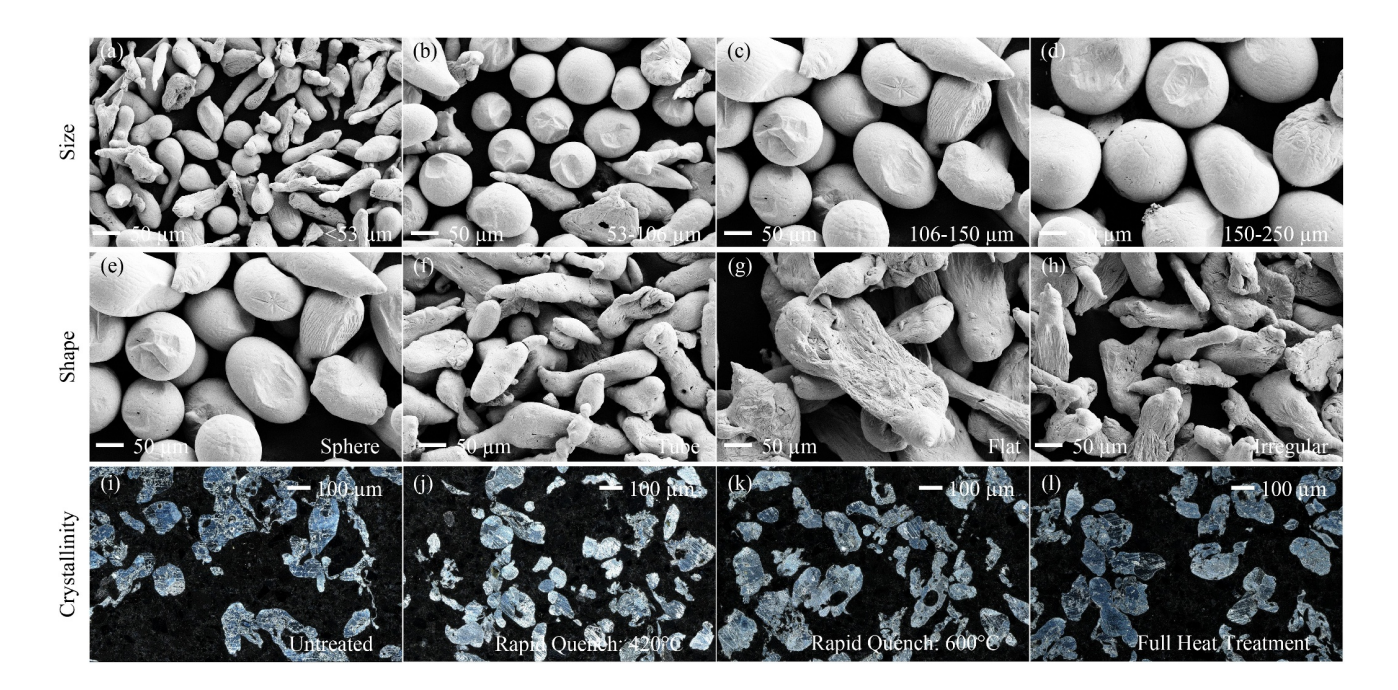


Fig. 1 Scanning electron microscopy (SEM) images of spherical particles representing the 4 size ranges: (a) $< 53 \mu m$; (b) $53-106 \mu m$; (c) $106-150 \mu m$; (d) $150-250 \mu m$ studied, SEM images of the four particle shapes studied: (e) sphere; (f) tube; (g) flat; (h) irregular, and metallography images representing the four particle heat treatments studied: (i) beginning with untreated; (j) RQT420; (k) RQT600; (l) FHT.

Additionally, a powder containing all particle shapes was selected as a control (Fig. S2). The four particle types were each sieved into size fractions, by stacking five sieves of decreasing size (3" Sonic Sifter Separator Sieve, Advantech Manufacturing, Inc., 53, 106, 150, and 250 μ m). This resulted in particle size ranges of > 250, 150–250, 106–150, 53–106, and < 53 μ m. Since all powder types contained a very small mass fraction of particle sizes larger than 250 μ m (Fig. S1), it was decided to remove the larger size fraction from the cohort of particle sizes studied, leaving four sieved fractions: < 53, 53–106, 106–150, and 150–250 μ m. SEM images of the particle size distributions are shown in Fig. S3, and Brunauer–Emmett–Teller (BET) surface area data for the sieved particle fractions are shown in Fig. S4.

Once the four powder shapes were sieved into adequate amounts of each size fraction, they were divided into four groups. The first group was not treated other than a rapid rinse with dilute acetic acid to remove any surface oxides, followed by drying. This group is denoted as "untreated." The remaining three groups were altered using a thermal recrystallization method developed in Lenhart et al. [41]. The thermal treatment consisted of three steps: oxide film formation, thermal grain growth, and oxide film removal. The steps for the oxide film formation and oxide film removal were identical for all powder size fractions undergoing thermal recrystallization and were detailed elsewhere in Lenhart et al. [41]. The last three groups varied in their cooling rate with the intent to manipulate the particle grain sizes; a plot of the thermal profiles for the three heat-treatments is provided in Fig. S5.

The recrystallizations were done in alumina crucibles in the center of a Carbolite Gero furnace in Argon (ultrahigh purity, Airgas) atmosphere. The furnace temperature was increased from room temperature to 100 °C at 10 °C/min and held for 1 h. The temperature was then increased from 100 to 600 °C at 10 °C/min and held for 1 h to melt the zinc in the zinc oxide shell. Then, the furnace was cooled from 600 to 420 °C at a rate of 2 °C/min. After annealing at 420 °C for 1 h, the furnace was cooled again at 2 °C/min to 25 °C. Lastly, the recrystallized powder was removed from the crucible, treated with dilute acetic acid to remove the oxide film, dried, and weighed. This method describes the "full heat treatment (FHT)" particles [41].

To introduce two more levels of varied crystallinity, powders were rapidly quenched from either 600 °C (RQT600) or 420 °C (RQT420) (Fig. S5). The quench was imposed once the target temperature was met by sliding the powder-containing crucible out of the hotspot of the tube furnace, exposing it to room-temperature gases inside the furnace, rapidly cooling the powder. Combining the 4 heat treatment variants (untreated, RQT420, RQT600, and FHT) with the 4 particle shapes (sphere, tube, flat, and irregular) and 4 particle size fraction ranges (< 53, 53–106, 106–150, and 150–250 μm), 64 powder variations were created.

2.2 Physical characterization and visualization

Zinc powders were imaged by both SEM and metallography. Powder samples visualized via SEM

(Zeiss Gemini500 FESEM) were immobilized on a standard sample peg with two-sided carbon tape and imaged directly at a working voltage of 15 keV. Powder samples visualized via metallography utilized one of two light microscopes (Zeiss AxioVert 200M and/or Keyence VHX-7000). Samples for metallography were first immobilized in a conductive carbon-based resin (PolyFast phenolic hot mounting resin with carbon filler), polished, and then acid etched to expose grain boundaries. The etchant consisted of a 1:1 volumetric ratio of HCl: water. The polished surfaces were exposed to the etchant for two seconds and then washed with copious amounts of deionized (DI) water (18.2 M Ω ·cm, Millipore Quantum TEX, Cat. NO QTUM0TEX1). The samples were then blow-dried with compressed air. Tap densities of the powders were measured by adding 50 g of zinc powder to a graduated cylinder and measuring the volume, after gentle tapping to facilitate particle packing. Texture coefficient data was produced by processing XRD patterns, which were collected using a Cu-sourced desktop XRD Rigaku (Rigaku Miniflex II Desktop X-Ray Diffractometer). The scan range was 20-100 degrees at a scan rate of 2 degrees per minute. The powder was immobilized on two-side scotch tape and placed on a Si P-type B-doped zero diffraction plate $(24.6 \text{ mm} \times 1 \text{ mm}).$

2.3 Slurry preparation

The composition of the zinc slurry was: approximately 70 wt.% (mass fraction) zinc powder, 30 wt.% pregel electrolyte, and ppm-level surfactant (proprietary). Pregel was prepared by mixing aqueous liquid electrolyte (30 wt.% KOH, 2 wt.% ZnO) with a polyacrylic acid (PAA) gellant. The pregel solution was mixed by shaking (Model DC-1-C Sport, The Miracle Paint Rejuvenator Company) for 15 min, allowed to rest for 24 h, and shaken a second time for 15 min. The zinc slurry anode was prepared by first thoroughly mixing the pregel and surfactant with a magnetic stirrer and then adding the zinc powder. The mix was shaken for 30 min, yielding the final slurry.

2.4 Electrochemical measurements

All electrochemical measurements were made using a Metrohm Autolab MAC80013 multichannel potentiostat. The *ex-situ* measurements were conducted in a custombuilt acrylic 3-electrode cell (illustrated in Fig. S6). The working electrode was an indium (In) foil (0.25 mm thick, 99.99%, Alfa Aesar) that was sealed to the bottom of the cell between two gaskets. The Zn powder or slurry was spread across the top surface of the foil within a small well. The reference and counter electrodes were zinc wire (1.0 mm in diameter, 99.5%, Alfa Aesar) and coiled nickel wire (Ni coil: 1.0 mm diameter, 99.5%, Alfa

Aesar), respectively. The electrolyte for all measurements was 30 wt.% KOH (NF/FCC Pellets, Macron) and 2 wt.% ZnO (Reagent plus, 99.9%, Sigma-Aldrich) dissolved in ultra-pure DI water.

Corrosion currents for powder form zinc were determined by linear sweep voltammetry (LSV). The zinc powders were allowed to rest in the electrolyte for 30 min while measuring a stable open circuit voltage (OCV) before beginning the experiment. The potential was swept from -100 to +100 mV vs. OCV at a scan rate of 0.2 mV/s. To extract corrosion current values (i_0) , an intersecting Tafel analysis was used with anodic and cathodic slopes equal to 120 mV/decade. For slurried zinc anodes, the corrosion current was extracted by linear polarization resistance (LPR). The slurries were allowed to rest for 30 min in the fully assembled cell, while measuring the OCV, before sweeping from +15 to -15 mV vs. OCV at a scan rate of 0.125 mV/s. The Stern-Geary equation was applied to extract corrosion current values (i_0) , again using Tafel slope values of 120 mV/decade for both halves of the redox couple. All corrosion current values were normalized to the mass of zinc. Achieved capacity measurements for zinc slurry and powder were determined by constant current discharge (CCD) at a rate of C/5 in the same acrylic cell. The target zinc mass on the working electrode was always 25 mg. Every experiment was done in triplicate, averaged, and is reported with standard deviation (σ) and coefficient of variation (C_{v}) values.

A subset of the zinc types was further investigated in an AA-replica cell having the same radial dimensions as a commercial AA battery but 1/4 the height [17]. This cell type provides a realistic operating environment, ensuring that the 3-electrode ex-situ behavior translates to real cells. Briefly, a thin layer of carbon nanotube ink (Tuball SWCNT 0.05% in 2-propanol) was spread on the inside surface of the cathode current collector and allowed to air dry before pressing in the commercial cathode pellet. Pre-rolled laminated cellulose separator paper was then inserted into a shallow well that held it in place while also allowing it to expand to touch the inside of the cathode pellet. Then, 240 µL of electrolyte was applied to wet the separator. Next, the cell was held under vacuum for 5 min. An anode current collector (tin-plated brass nail) was inserted into the center of the assembly. Lastly, freshly prepared zinc slurry was pipetted into the anode compartment and the cell was sealed with a transparent acrylic top. The OCV of the assemblies was measured (around 1.6 V) to ensure proper assembly before performing a CCD at C/20.

2.5 Statistical analysis

The statistical analyses to identify the most significant factors impacting the corrosion current and achievable capacity were conducted utilizing Minitab 18. A 4^k DOE

matrix was constructed in the software where 4 represents the number of levels considered for each factor (k). The three factors considered were particle size, particle shape, and particle crystallinity. The four levels for particle size were < 53, 53-106, 106-150,and 150-250 μ m. The four levels for particle shape were sphere, tube, flat, and irregular. The four levels for crystallinity were untreated, RQT420, RQT600, and FHT. A concise representation of the 64 particle-type matrix can be found in Fig. S7. Data was entered in triplicate for achievable capacity (mAh/g) and corrosion current (mA/g) measurements and analyzed in the Minitab DOE matrix. The resulting output for each were Pareto and main effects plots (shown for all cases in this document) as well as the quality of data residuals (shown for all cases in the ESM). The values reported in the main effects plots are statistical averages of each measured corrosion and achievable capacity of each factor and then plotted

numerically by factor to elucidate general trends. Therefore, values reported in main effects plots do not come from one single sample, but rather a series of averages compared to one another using a factorial-based algorithm.

3 Results and discussion

3.1 *Ex-situ* corrosion and achieved capacity of zinc powders

The behavior of powder zinc in zinc-alkaline batteries is complicated due to the multitude of components comprising a slurried zinc anode. Therefore, this work began by measuring the corrosion current and achievable capacity in the powder form exposed to liquid alkali. Figure 2 shows representative LSVs for the spherical

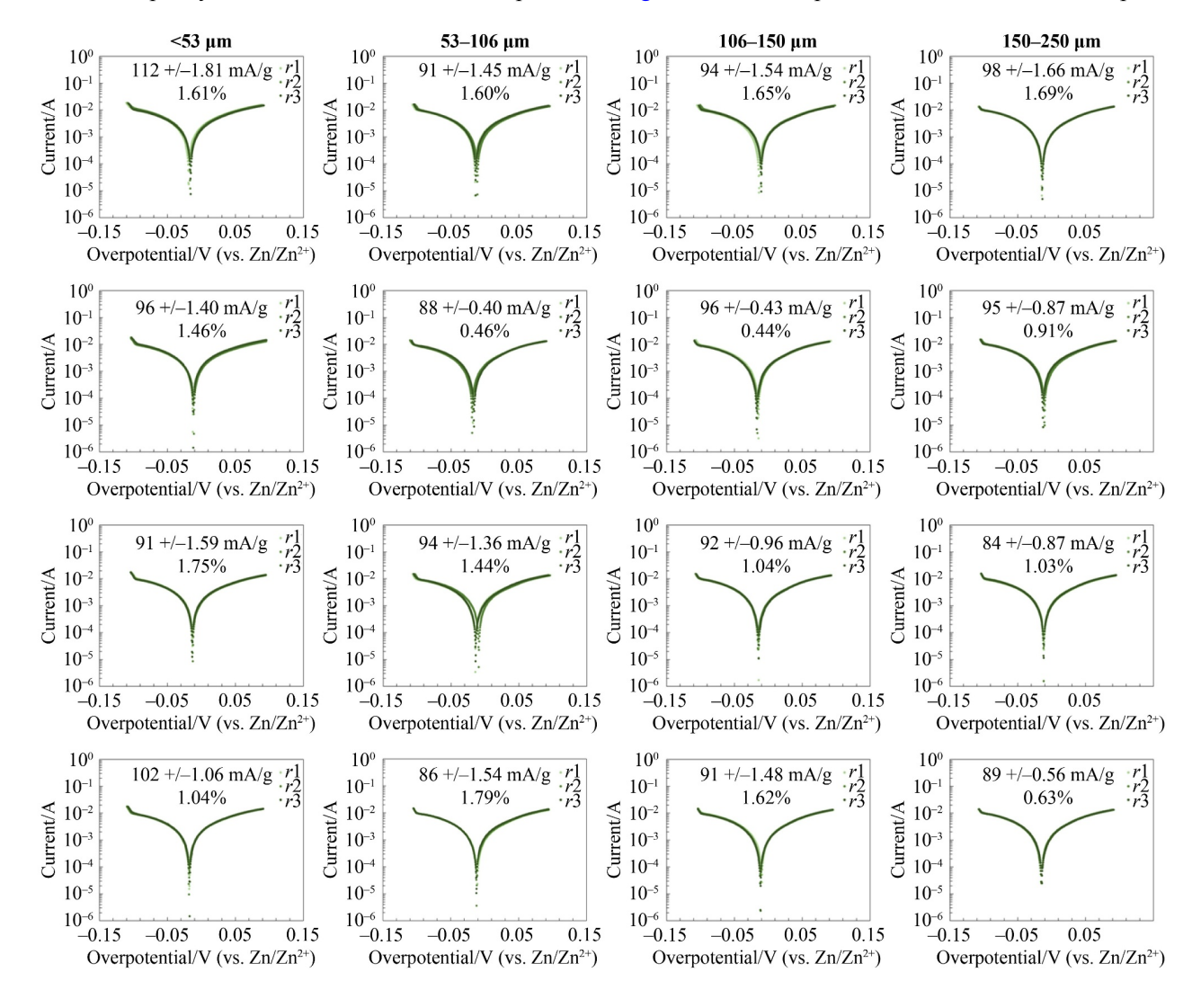


Fig. 2 Triplicate LSV data for spherical particles in powder form (gravimetrically normalized corrosion current values are reported with their standard deviation values adjacent and coefficient of variation percentages underneath. Rows represent different heat treatments imposed on the particles and the columns represent the different size fractions).

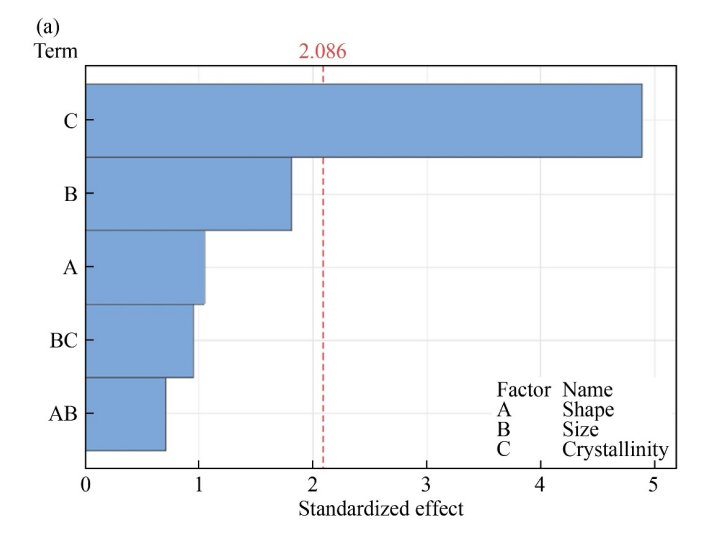
particle type, partitioned into size fraction ranges (columns) and varying heat treatments (rows). Identical data sets for tube, flat, and irregularly shaped particles can be found in Figs. S8–S10, respectively. All of the LSVs had the expected shape, with an initial sharp slope near the open circuit potential, and then a log-linear (Tafel) region where the slope on each side was approximately 120 mV/decade. The average specific corrosion current, standard deviation, and the coefficient of variation are inset to each panel. They are also tabulated in Tables S1–S4 for all particle types.

To better understand the influence of the factors on the corrosion current with such a large data set, following the data collection and extraction of corrosion current values, Minitab 18 was used to perform a 4^k factorial statistical analysis. Figure 3 shows the primary output plots from the analysis, a Pareto chart (Fig. 3(a)) and a main effects plot (Fig. 3(b)). The Pareto chart identifies which of the factors (shape, size, and/or crystallinity) are statistically significant on the measured parameter (corrosion current) and main effects plots show the averaged effect for each factor, broken down into its four corresponding sublevels. A quality of data residuals plot can be found for this data set in Fig. S11.

The Pareto chart shows that the only statistically significant parameter (95% confidence interval) for corrosion was the zinc crystallinity (Fig. 3(a)). This was surprising, particularly for particle size, because it was anticipated beforehand that the greater surface area of smaller particles would facilitate more corrosion than the same mass of larger particles. But it is also important to consider that the large particles are generally both more porous than the smaller particles, increasing surface area, and they also have more total grains and grain boundary

area, facilitating a greater extent of inter-granular corrosion. The main effects plot supports the Pareto chart by showing that the highest corrosion current values were the untreated particles with an averaged value of 102 mA/g. The three variations of heat-treated (FHT, RQT420, and RQT600) particles all had an average corrosion current value of approximately 93 mA/g, resulting in an approximately 10% reduction in corrosion current when compared to the untreated case. Another outcome of the analysis was the observation that the corrosion current was insensitive to the heat treatment temperature and cooling rate (within the data set). This can be linked back to the grain states of rapidly quenched particles at 420 °C (RQT420) and 600 °C (RQT600). It was observed that these particles had comparable grain sizes to the FHT particles (Figs. 1(j)-1(1)). This observation implies that the cooling rate used to quench the melted powder is slower than the recrystallization kinetics and, thus, all three cooling processes are sufficient after annealing at 600 °C.

To measure the achievable capacity of zinc powder, CCD experiments were performed at a C/5 rate. Though a C/5 discharge rate is fast for these types of anodes, this C-rate was chosen for rapid data acquisition and agreement with standard "flashlight tests" which are about 8–10 h continual use experiments. Figure 4 shows the capacity measurements for spherical particles organized by particle size (columns) and heat treatment (rows). Identical figures for tube, flat, and irregularly shaped particles are given in Figs. S12–S14, respectively. Since these discharge plots were recorded in a 3-electrode cell of zinc powder as the working electrode and zinc wire as the reference, the OCV was expectedly low. As the working electrode is anodically polarized, the relative



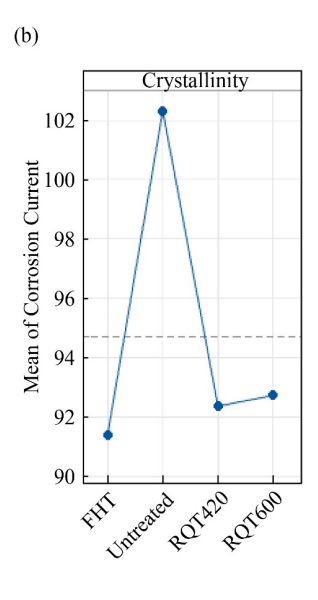


Fig. 3 Minitab output plots from statistical analysis of corrosion current data of powder zinc in liquid electrolyte.

(a) Pareto chart showing the statistical significance for size, shape, and crystallinity on the corrosion of powdered zinc; (b) main effects plots for the only statistically significant factor, crystallinity, broken down into its four sub-levels.

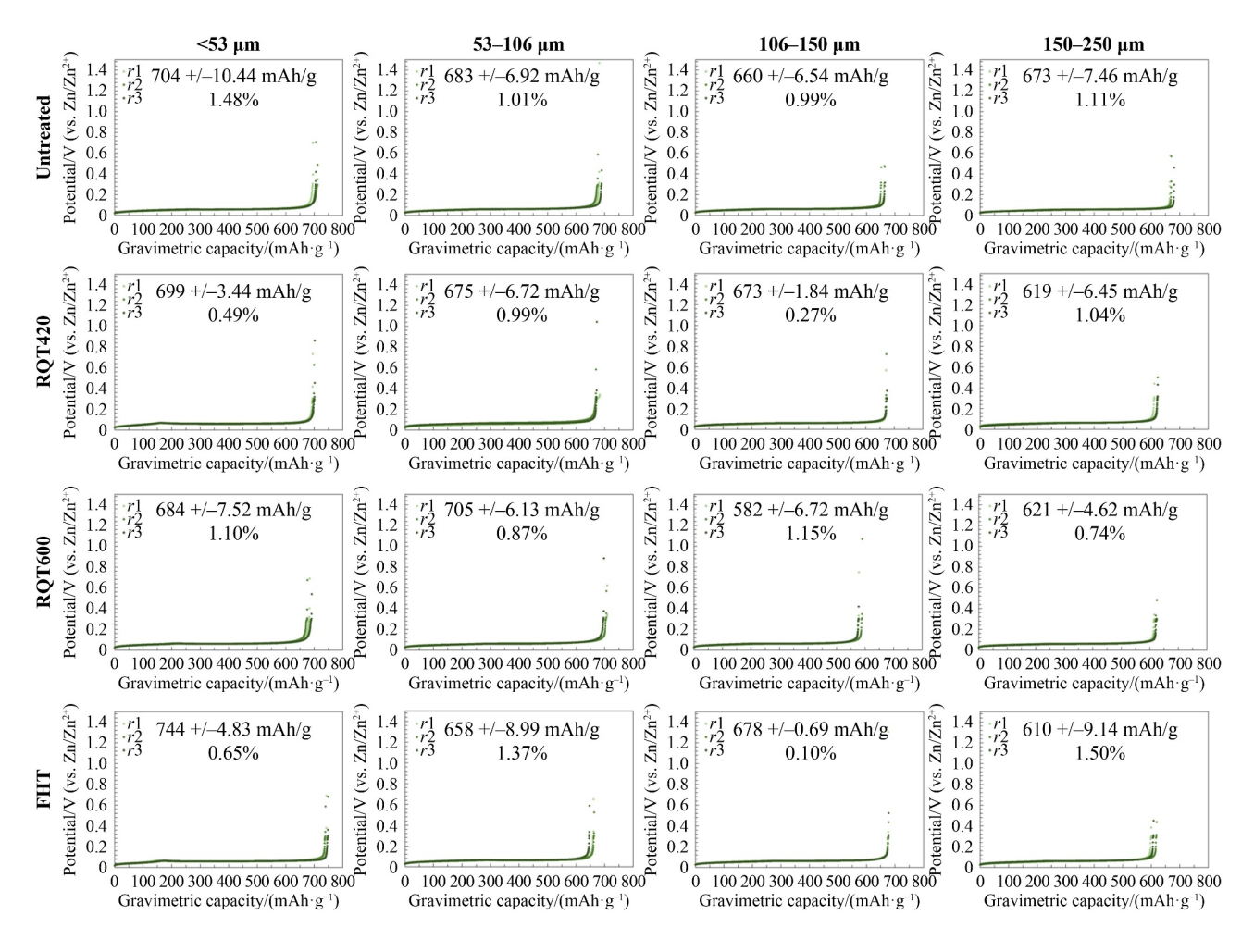


Fig. 4 Triplicate CCD data for spherical particles in power form (gravimetrically normalized achievable capacity values are reported with their standard deviation values adjacent and coefficient of variation percentages underneath. Rows represent different heat treatments imposed on the particles and the columns represent the different size fractions).

potential of the zinc powder will increase relative to that of the quasi-stable zinc reference. This increase in polarization is initially due to concentration polarization throughout the porous anode bed via hydroxide anion consumption in the zinc dissolution process, which causes a rapid increase in overpotential of about 50 mV. This initial spike in voltage is followed by a plateau region of steady voltage decay caused by the steady dissolution of zinc beginning at the top of the anode (initially pageion mass-transport limited) moving downward toward the current collector. While in the plateau region, critical saturation levels of zincate are achieved and the spontaneous nucleation of zinc oxide (passivation) is observed, leading to greater anode polarization and increased tortuosity for hydroxide anion transport through the nucleated ZnO to the underlying electroactive zinc surfaces [42]. Eventually, the overvoltage increases rapidly due to complete electroactive surface passivation; the potential turns asymptotically vertical, and indicates the extent of the achieved capacity for the powder. Zinc has a theoretical capacity of 820 mAh/g whereas the achieved capacities of powders

studied in this work were typically 600–700 mAh/g, suggesting an overall reasonable utilization and that a C/5 rate was not too fast for these studies.

Upon closer examination of the achieved capacity plots in Fig. 4, a general trend can be observed for particle size: higher achieved capacity with decreasing particle size. This trend was observed for sphere, flat, and irregular geometric particle shapes studied. Only tube shaped particles appeared to lack this behavior. A comprehensive list of all achievable capacities (mAh/g) for all particle shapes, sizes, and crystallinities in terms of average (mAh/g), standard deviation (±mAh/g), and coefficient of variation are tabulated in Tables S5-S8 (grouped by sphere, tube, flat, and irregular shaped particles, respectively). As with the corrosion current data, to provide a statistically meaningful interpretation of the large amount of data collected, achieved capacity values were analyzed with Minitab 18. The Pareto chart and main effects plots for achievable capacity can be seen in Fig. 5. Using a 95%, two-sided confidence interval, it was revealed that the two statistically significant factors contributing to achievable capacity were the particle size

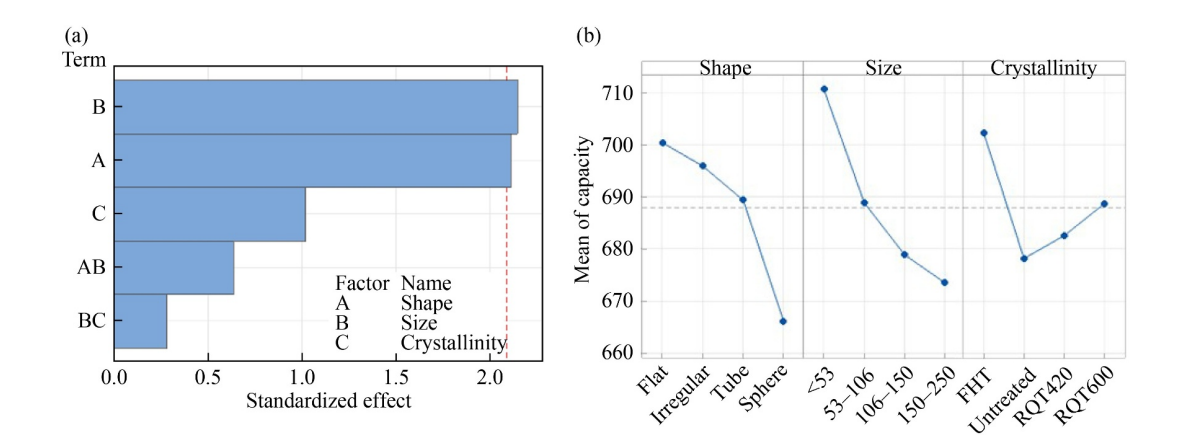


Fig. 5 Minitab output plots from the statistical analysis of achieved capacity data for powder zinc in liquid electrolyte.

(a) Pareto chart showing the statistical significance for size, shape, and crystallinity on the achieved capacity of powdered zinc; (b) main effects plots for each of the primary variables, broken down into their four sub-levels.

and particle shape, but not crystallinity. Residuals for the quality of data can be found in Fig. S15.

At first, the finding that crystallinity did not have a statistically significant effect on capacity appears to be contradictory to our previous work that showed an increase in achievable capacity with increased crystallinity [41]. What it points to is the complexity in differentiating between the types of heat treatments across multiple particle shapes and sizes. Looking at the main effects plots in Fig. 5(b), all the mean values for the achievable capacity for heat treated particles are greater than the untreated particles. The excellent agreement between the model and data (Fig. S11) also shows that even though the crystallinity (some heat treatment vs. no heat treatment) may in fact influence capacity, that effect is smaller in comparison to the other performancecontributing factors like particle size and shape. Under high polarization conditions (discharge), zinc dissolution occurs at the metal-electrolyte interface rather than along grain boundaries (where corrosion is known to occur). This is because at higher discharge rates, the intergranular diffusion time constant is much slower than migration. Further, the higher degree of organization of a reconstituted zinc crystal can facilitate more uniform dissolution and current density distribution, thereby improving the performance of the anode, but that effect is likely smaller in comparison to other particle factors like size and shape.

Turning to the effects of particle size, the main effects plot in Fig. 5(b) shows a clear trend where smaller particles perform better than larger particles in terms of measured achievable capacity. The size phenomenon can be explained by the fact that small particles have greater surface area-to-volume ratios and therefore have a greater ECSA than their larger particle counterparts, leading to a greater number of reaction sites per mass, more facile dissolution kinetics, and lower overall polarization of the electrode, all contributing to the improvement in

capacity. Further, larger particles suffer from pore plugging via premature passivation, reducing material utilization and, consequentially, anode performance. The locally rapid accumulation of zincate and depletion of hydroxide anions proximal to the lower surface area large particles, combined with a larger activation polarization and higher areal current density, facilitates passivation, reducing performance in a way that smaller particles with larger net ECSA are less prone to.

The main effects plot in Fig. 5(b) suggests that the best performing particle shape was flat, followed by irregular, tube, and sphere. The flat, tube, and irregularly shaped particles performed comparably well to one another. It is worth noting that the spherical particles are exceptionally smooth with a low degree of porosity in comparison to the other particle shapes tested (Fig. S3 (SEM images) and S4 (BET surface area measurements)). In a powder stack, spherical particles of any size will pack together well. The other geometric particle shapes have fine particles packed together well, but as the size of the nonspherical particles is increased their tap-density decreases (Fig. S16). A reduction in powder stack tap density with larger particles implies that the anode will be physically thicker for a given mass loading of zinc, leading to increases in the Ohmic and mass transport resistances and performance loss. In contrast, small particles of nonspherical geometric shape are likely to have a greater number of points of contact between them due to the large number of protrusions and recesses that can interlock with one another in comparison to smooth spheres. Particles shapes with greater numbers of points of contact can perform exceptionally well likely due to their extensive network of electron conductive paths, which decreases the need for the complex redox-shuttling mechanism known to occur in zinc-alkaline systems [17,43]. In contrast, particle stacks with fewer contact points are less electronically conductive and have a greater resistance in electron transport, increasing the necessity of redox shuttling to facilitate discharge. This increase in complexity in material utilization associated with the particle shape may lead to a reduction in achieved capacity in spherical powder stacks. In contrast, the slurries used in real cells have Zn particles that are nearly totally dispersed in the electrolyte, meaning that for all particle shapes very few particles are ever in physical contact. This forces the zinc discharge to rely almost exclusively on the redox-electrolyte shuttle mechanism to move electrons and ions in the anode which is a significantly different mechanism of electron and ion conduction within a discharging, porous, totally electronically percolated, stack of powder particles resting on top of one another via gravity in a liquid milieu [17]. This difference in the discharge dynamics likely causes the behavior in slurry form, studied in the next section, to deviate somewhat from what was observed in the powder form in this section, particularly relating to the achievable capacity.

A final important consideration is how the particle morphology changes as the discharge proceeds. Because of the differences in packing and discharge, spherical particles likely change their shape more readily than the other shapes. This is shown in Fig. S26 alongside a brief discussion. It is shown that the particle morphology indeed changes at various depths of discharge (DoD), where particles tend to retain their overall morphology at low DoD, but become highly pitted and lose shape at high DoD. Additionally, passivating ZnO (identified both visually by SEM and with X-ray diffraction) becomes much more prevalent as the DoD increases.

3.2 *Ex-situ* corrosion and achieved capacity of slurried zinc

The zinc anode in alkaline batteries is complex, using a slurry-based electrode that is affected by more sophisticated kinetic and mass transfer processes than the percolating powder-in-liquid cases studied above. Therefore, it is necessary to also investigate the behavior of powder zinc in slurried anodes to determine whether the same variables are controlling corrosion and discharge behavior in the gelled electrolyte environment. Since it was confirmed in Section 3.1 that rapidly quenching zinc during the recrystallization step yielded the same grain growth as slow, controlled cooling, the analysis matrix (Fig. S17) was simplified for the slurries — only untreated and FHT powders were considered. For measuring the corrosion currents of zinc slurries, LPR was used instead of LSV due to concentration polarizations that are observed in the viscous gel under the high overpotential conditions native to the LSV technique. LPR utilizes small overpotential (low field theory) that requires the experimenter to use the slope of the I-V plot to calculate corrosion current values via the Stern-Geary equation. For all the zinc slurries, the corrosion current values were normalized to the mass of zinc in the slurry. Figure 6 shows representative LPR plots for slurry zinc electrodes for spherical particles grouped by heat treatment (rows) and particle size (columns). LPR plots for tube, flat, and irregular shaped particles can be found in Figs. S18-S20. The full set of extracted mass-normalized corrosion current values for each particle type (average, standard deviation, and coefficient of variation) can also be found

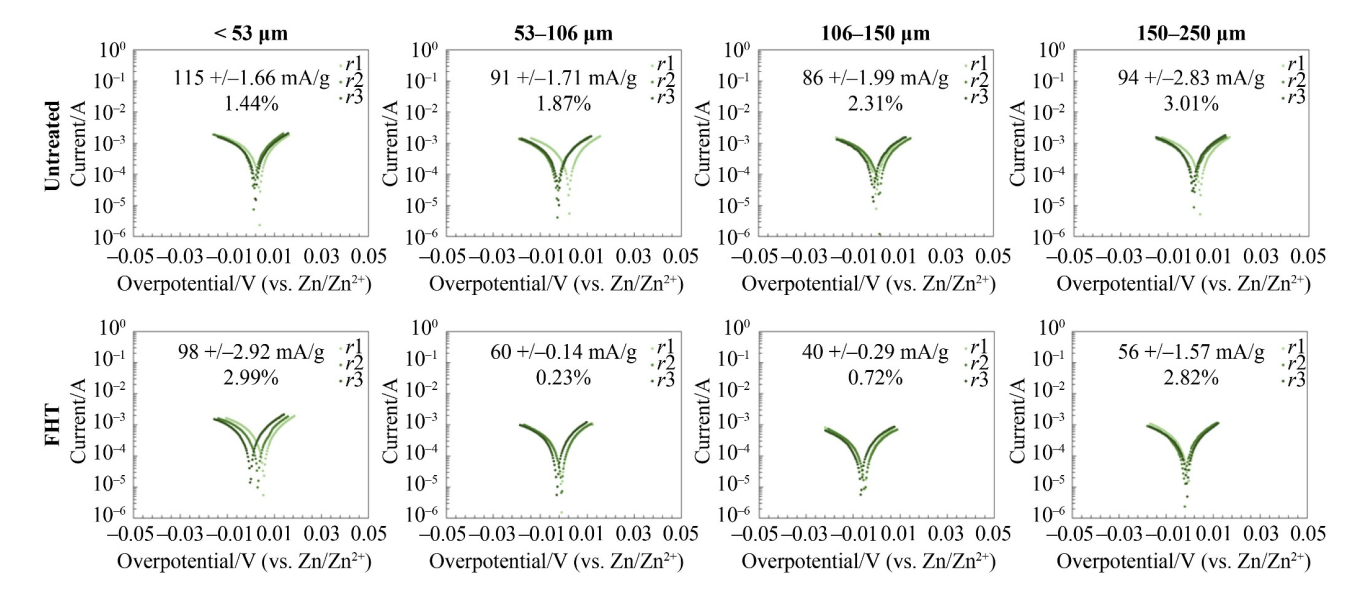


Fig. 6 Triplicate LPR data for spherical particles in slurry form (gravimetrically normalized corrosion current values are reported with their standard deviation values adjacent and coefficient of variation percentages underneath. Rows represent different heat treatments imposed on the particles and the columns represent the different size fractions).

in Tables S9-S12.

When comparing the untreated spheres to the FHT spheres in Fig. 6, a significant reduction in corrosion current was observed for the FHT row for every size fraction. Additionally, there appeared to be a clear relationship between particle size and corrosion smaller particles having significantly higher corrosion values than larger particles for both FHT and untreated samples. This trend with particle size and corrosion was not reflected for all particle shapes, though, and this observation is conclusively noted in the statistical analysis output of Fig. 7. Figure 7(a) shows the Pareto chart for statistically significant parameters (95% confidence interval) with particle crystallinity and geometric particle shape being the most contributive to the measured corrosion currents, followed by the combined effects of particle shape-and-size and particle size-and-crystallinity, and then particle size. As was seen with powder zinc in liquid electrolyte, crystallinity is the primary driver for corrosion, demonstrating again that increasing the size of the zinc grains can result in an overall reduction in corrosion. Interestingly, particle shape and size also play significant roles in influencing corrosion in the gelled electrolyte environment. This is in contrast with the results from the corrosion analysis on a zinc powder stack in liquid electrolyte, which can likely be explained by mass transport effects that are present in the gelled electrolyte. When the zinc is slurried, the viscosity of the gelled electrolyte reduces ionic conductivity and creates concentration polarizations that are otherwise absent in a low viscosity liquid electrolyte. Since concentration polarizations build more easily in viscous media, factors like particle shape and size begin to play more important roles in driving or suppressing corrosion.

It is also possible that the PAA microgel particles of the highly viscous electrolyte do not extensively penetrate the smaller pores of particles or along their grain boundaries. Fully swollen PAA microgel particles are known to get as large as 25 µm in diameter in this highly alkaline electrolyte (pH = 15) which totally neutralizes all carboxylic acid functional groups of the PAA polymers. This maximizes the electrostatic repulsion of deprotonated carboxylic acid moieties, inducing swelling. Grain boundary thicknesses (distance between neighboring grains within a particle) generally do not exceed several nanometers and consequentially fully swollen PAA microgel particles can spatially exclude corrosive electrolyte from creeping in. Binary interactions between particle shape-and-size and particle size-and-crystallinity also are statistically significant though these higher-order interactions can be difficult to interpret directly and more elaborate means of elucidating their mechanisms of interaction is necessary.

Looking at the main effects plot in Fig. 7(b), it can be seen that the average untreated particle has an approximately 25% larger corrosion current value, 120 mA/g, than the recrystallized FHT group, 90 mA/g. Further, the most corrosive particle shapes were irregular and flat at 120 and 115 mA/g, respectively. Tube shaped particles had an average corrosion current value of 100 mA/g and spherical shaped particles had the lowest reported average of approximately 80 mA/g. It is worth noting that the spherical particles are exceptionally smooth and less porous than the other shapes studied. SEM (Fig. S3) showed that flat and irregularly shaped particles have considerable surface roughness. When considering particle size and its effects on corrosion current in slurried anodes, there is a general trend that can be seen in all the particle shapes where small particles (< 53 and 53–106 µm) have higher average corrosion current values than large particles (106-150 and 150-250 µm). These results make sense since smaller particles have larger surface area-to-volume ratios than larger particles and

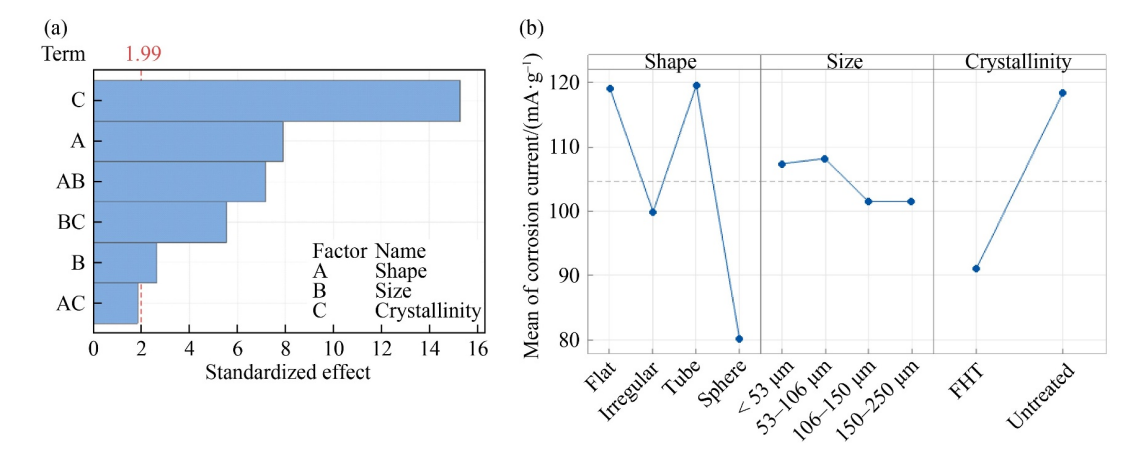


Fig. 7 Minitab output plots from statistical analysis of corrosion current data of zinc slurries.

- (a) Pareto chart showing the statistical significance for size, shape, and crystallinity on the achieved capacity of zinc slurry anodes;
- (b) main effects plots for the statistically significant shape and crystallinity factors broken down into their corresponding sub-levels.

concentration polarizations are more intensely felt in slurry. Comparing the analysis output of the slurry corrosion data to the powder corrosion, the primary driving factor for corrosion in both powder and slurry is the crystallinity of the particle — larger grained particles corrode less than smaller grained particles.

Turning attention to slurry discharge performance, Fig. 8 shows CCD plots of slurry zinc for spherical particles, grouped by heat treatments (rows) and particle sizes (columns). Discharge plots for tube, flat, and irregular shaped particles can be found in Fig. S22–S24 and residuals for the analysis in Fig. S25. The averaged capacity values with standard deviations and coefficients of variations are tabulated in Tables S13–S16. Figure 9(a) shows the Pareto chart for slurry zinc CCD data, showing

that the two most statistically significant factors toward achieved capacity are particle shape and particle size, with the binary interactions of these two particle features ranking third in statistical significance. This Pareto output for slurry is consistent with the powder achievable capacity, with the exception that the particle shape and size standardized effects are more pronounced when slurried. This is supported by the main effects plot for particle size in Fig. 9(b), where the smaller particle sizes (< 53 and 53–106 μ m) with average achievable capacity values of 725 mAh/g outperform the larger particles (106–150 and 150–250 μ m) with average achieved capacity values of 700 mAh/g. When comparing particles with varied shapes in Fig. 9(b), sphere, irregularly, and flat shaped particles are the best performing with

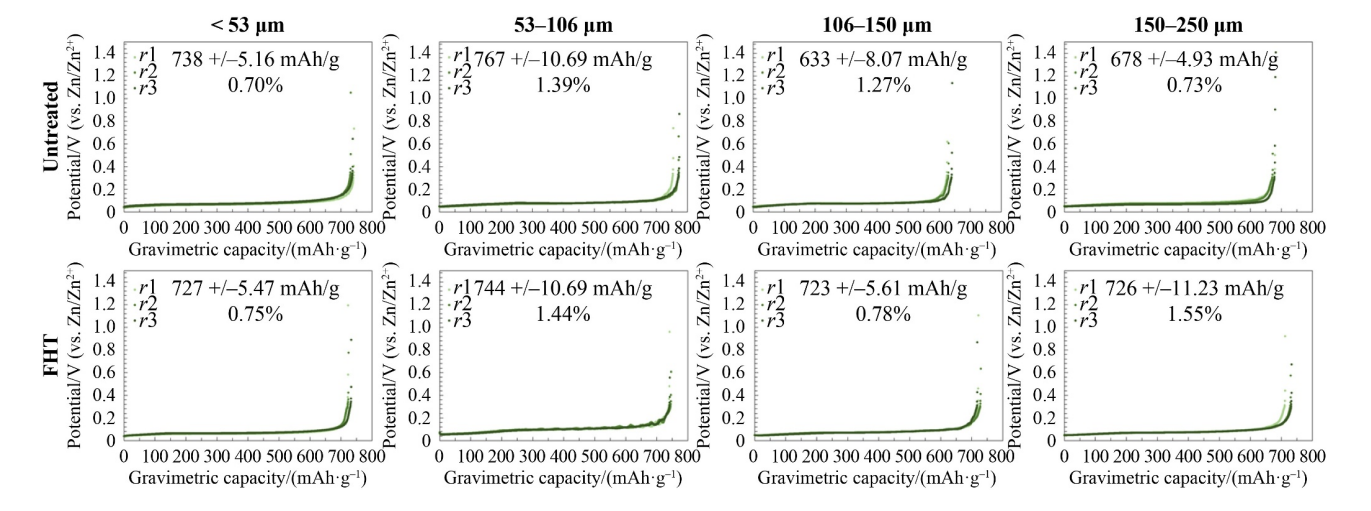


Fig. 8 Triplicate CCD data for spherical particles in slurry form (gravimetrically normalized achievable capacity values are reported with their standard deviation values adjacent and coefficient of variation percentages underneath. Rows represent different heat treatments imposed on the particles and the columns represent the different size fractions).

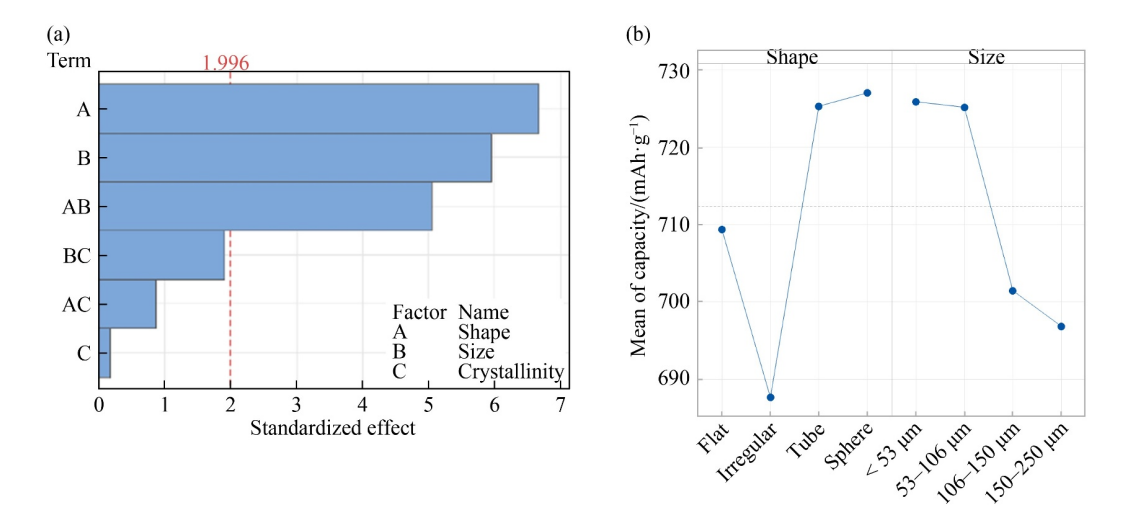


Fig. 9 Minitab output plots from statistical analysis of achieved capacity of zinc slurries.

- (a) Pareto chart showing the statistical significance for size, shape, and crystallinity on the achieved capacity for zinc in slurry form;
- (b) main effects plots for the statistically significant shape and size factors broken down into their four sub-levels.

averaged achieved capacity values around 727, 725, and 710 mAh/g, respectively. The tube shaped particles are the worst performing particle shape in slurry, with an averaged value of 688 mAh/g.

When comparing slurries to the powder-liquid achievable capacities measured in Section 3.1, similar trends with particle size are observed. Smaller particles are consistently better performing than larger particles in either liquid media or gelled. This observation can likely be explained by the electrode polarization needed to facilitate a particular dissolution rate. Smaller particles have larger surface area-to-volume ratios and generally greater ECSA than a larger particle with a lower ECSA (Fig. S4). The rate of dissolution depends on the availability of active sites on the electrode surface, which is proportional to the ECSA. An electrode with high ECSA has more active sites and a lower current density, which can accommodate higher rates of electrochemical reactions and lower anode polarizations compared to a low ECSA anode.

On the other hand, the trends in particle shape were quite different between slurries and powder-liquid systems. The main effects plot in Fig. 9(b) indicates that spherical and irregular shaped particles were the best performing in slurry, followed by flat and then tube shaped. In contrast, it was observed that in a powder stack the best performing particle shapes were flat (planar) and irregular followed by tube and sphere. Spherical particles were the worst performing in powder-liquid but the best performing in slurry. This is likely caused by differences in surface accessibility, particle-to-particle contact and a number of other differences in the anode structure between zinc powder stacks and zinc slurries noted in earlier discussion.

In addition to slurry zinc particles being fully dispersed and suspended by gel electrolyte, standard slurries often include small amounts of organic additives/surfactants that enhance the performance of the anode by facilitating discharge, preventing corrosion, and delaying formation of insulating passivating films. The role of surfactants (type and loading) is beyond the scope of this paper, but it will be the focus of future work by our group. Additionally, the slurry composition (Zn mass fraction, KOH concentration, ZnO concentration, etc.) can also impact the corrosion and discharge dynamics in commercial anodes and will also be studied and reported later.

3.3 *In situ* analysis of down-selected zinc powders in an AA-replica cell

Although the *ex-situ* results provide insight into the effects of zinc particle features on corrosion and capacity, it is also important to study zinc in a realistic reacting environment that simulates commercial batteries. Custom-built AA-replica cells have been engineered and

deployed in Faegh et al. [17–19] and are utilized here. An AA-replica cell with a control zinc powder (comprised of multiple particle shapes and sizes) as the slurry anode was used as a reference (Fig. 10(a), red line). The control anode was able to achieve a capacity of 290 mAh/g. Based on the results in Sections 3.1 (powder) and 3.2 (slurry), where both analyses showed that particle size and shape were statistically the most significant in driving capacity performance, two cohorts of AA-replica cells were assembled. The first cohort of AA-replica cells tested were < 53 µm with three different-shaped (sphere, flat, and irregular) zinc particles (Fig. 10(a)). The < 53 µm sphere Zn performed the best with an achievable capacity of 435 mAh/g. The < 53 µm irregular shaped Zn (397 mAh/g) and the < 53 μ m flat Zn (335 mAh/g) both outperformed the control. These in-situ results agree well with the ex-situ CCD slurry results where sphere shaped particles were the best performing, followed by irregular and flat shaped particles.

Post-mortem optical images, showing a birds-eye view of the anode column through the acrylic top of the cell, can be seen to the right of the discharge plots (Figs. 10(b)-10(e)). The fineness of the $< 53 \mu m$ particles (Figs. 10(c)-10(e)) is apparent compared to the control anode (Fig. 10(b)) containing the entire range of particle sizes. Another important set of information that can be taken from these images is the discharge state of Zn. When a zinc anode is discharged, different colors become visible, corresponding to different physical properties of the Zn itself. These colors and their connection to the electrochemistry have been extensively characterized by other researchers via SEM, XRD, and EDS [17,19,42,44]. Briefly, blue coloration is indicative of zincate, combined with a Type I zinc oxide film. This Type I zinc oxide film is a loose flocculant layer through which ions and water can move and is produced through a dissolutionprecipitation reaction process as the result of a supersaturation of the aqueous ion discharge product, zincate. This film forms first around particles at the separator in electrolyte space, intensifying in color and moving radially inward toward the current collector over time. The white annulus just within the blue is the formation of a large abundance of Type II zinc oxide, which forms a passivating layer that inhibits reactant and ion mass transport. The Type II zinc oxide layer is a coherent layer formed directly on the surface of the particle and is produced through the direct surfaceoxidation of metallic zinc under high overvoltage situations, generally toward the end of the anode life. Type II zinc oxide is characterized as a thick crust in direct contact with the underlying metallic particle, forming a completely ionically insulating layer. Moving deeper, a distinct black ring can be observed, comprised of high surface area metallic zinc [17] that is formed under the most constrained mass transfer conditions. Finally, the center of the anode is primarily comprised of

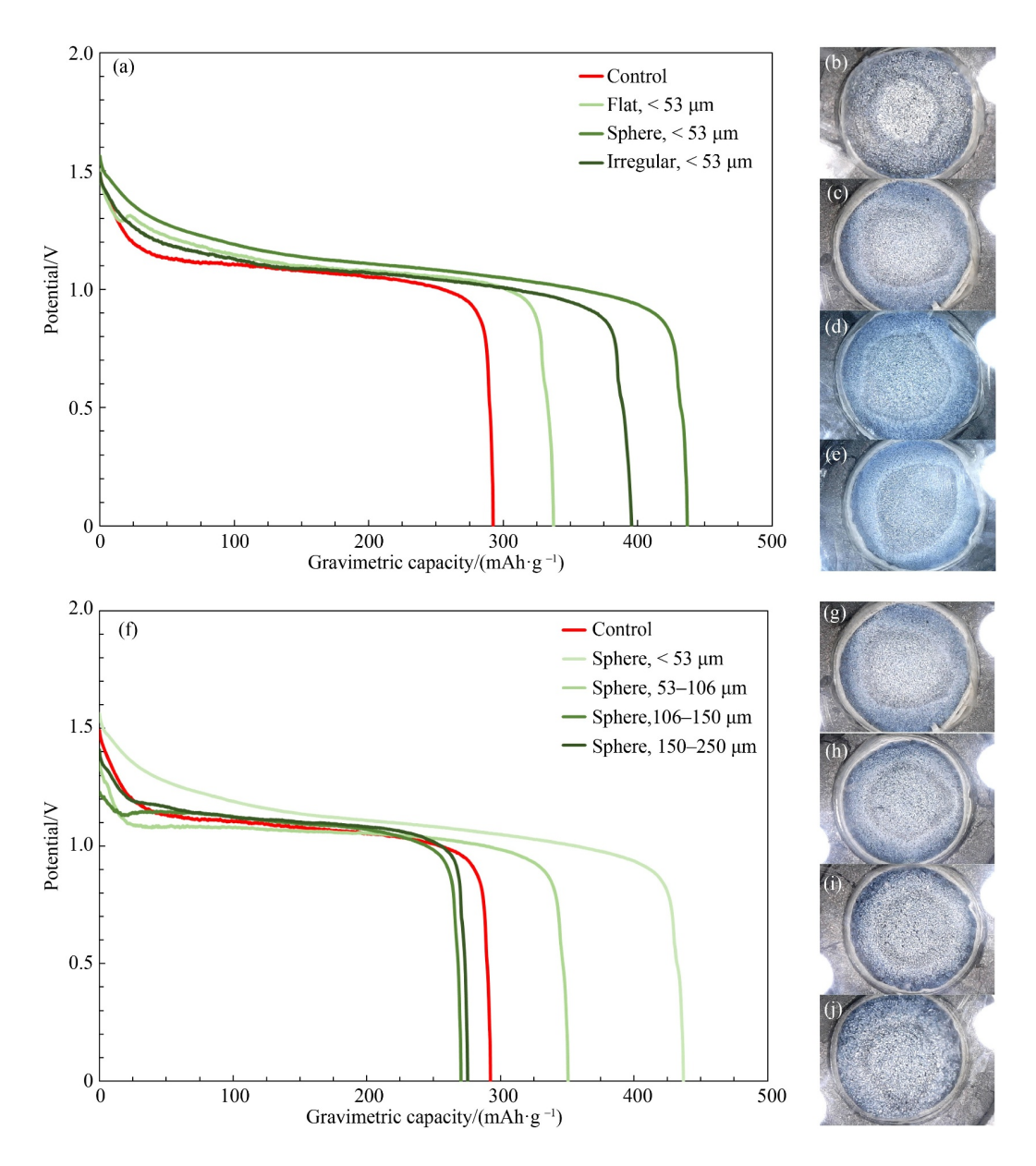


Fig. 10 In situ experiments for select Zn powders in slurry form.

(a) Discharge plots for $< 53 \mu m$ size fractions of sphere, flat, and irregular shaped particles in AA-replica cells compared to a control (red) Zn powder comprised multiple particle shapes and sizes; (b–e) optical images showing a birds-eye view of the AA-replica cells post-discharge with control, $< 53 \mu m$ sphere, $< 53 \mu m$ flat, and $< 53 \mu m$ irregular particles, respectively; (f) discharge plots for the best performing particle shape (sphere) for multiple size fractions: < 53, 53-106, 106-150, and $150-250 \mu m$; (g–j) optical images showing a birds-eye view of AA-replica cell post-discharge with spherical particles of sizes < 53, 53-106, 106-150, and $150-250 \mu m$, respectively.

undischarged zinc particles (metallic gray), though some Type I and Type II Zn can also be present there.

The second cohort of AA-replica cells consisted of zinc slurries prepared from spherical powders with < 53, 53–106, 106–150, and 150–250 μm sized particles, whose discharge profiles are shown in Fig. 10(f). Briefly, the < 53 μm zinc anode was the best performing at 435 mAh/g, followed by 53–106 μm with an achieved capacity of 350 mAh/g. The large particle fractions of 106–150 and 150–250 μm did nearly equally poor with achieved capacity values of 270 and 275 mAh/g,

respectively. These larger particle fractions performed worse than the control (297 mAh/g), which contained both large and small particles. Post-mortem images of the spent zinc anodes can be seen to the right (Figs. 10(g)–10(j)). The pattern of annuli observed in these anodes is similar to the first cohort, except for the larger particle zinc anodes (53–106, 106–150, and 150–250 µm) where the dark black center is replaced with a distinct black ring and dense white center, like the control. For the < 53 µm anodes, working radially inward from the separator-anode interface a dark blue outer anulus (Type I ZnO), a

dense white anulus (Type II ZnO), and then a dark black ring and gray-to-nearly black center (undischarged zinc particles and Type II ZnO) are observed. In contrast, the control anode follows the same color pattern, but the gray center is replaced with a dense-appearing white center. The fact that the fine particle anodes turn dark gray to black but the larger particle anodes turn white suggests a difference in species distribution and dissolution mechanism throughout the anode as it is discharged. Generally, dense white is associated with passivation and black is associated with the formation of redox-shuttle product, high surface area black zinc [17]. The lack of obvious extensive passivation in the center area of the fine particle anodes is likely the reason for their better performance. The results in the AA-replica cells are exactly consistent with the ex-situ slurry analysis, suggesting that the ex-situ platform can be used to obtain data that can translate into in-cell performance with very little material, allowing for the rapid screening zinc particle types and configurations in the future.

4 Conclusions

In this paper, the corrosion and achievable capacity were measured for powder and slurry Zn using both ex-situ and in-situ electroanalytical platforms. 64 different types of Zn were rapidly screened. DOE matrices were organized to study fundamental derived properties of the zinc particles based on their shape, size, and crystallinity. Based on a statistical analysis, it was concluded that the most statistically significant particle property driving corrosion was crystallinity, where increased crystallinity led to reduced corrosion. The crystallinity was manipulated by heating the Zn particles in an oxide shell to melt them followed by cooling (where the cooling rate did not influence the crystallinity). For discharge capacity, more complex dynamics in slurry versus powder-in-electrolyte led to slightly different results that could be explained by the differences in electrical contact and mass transfer in the two environments. In general, smaller particle sizes achieved higher capacities and the particle shape was also statistically significant. The results here can be used to inform the design of Zn for both aqueous and gelled electrolyte applications, such as Zn alkaline batteries. This paper shows that a simple, inexpensive, 3-electrode platform can be used to systematically screen milligram quantities of material and produce results that translate into real cell improvements for a fraction of the time, personnel, material, and cost. Traditional industrial cell builds to study these properties in real AAs cost many thousands of dollars, a large amount of Zn to be produced, and require significant other resources, time, and teams of trained professionals.

Electronic Supplementary Material Supplementary material is available in the online version of this article a https://doi.org/10.1007/s11708-024-0904-1.

Competing Interests Financial conflicts of interest may exist for MZ and MH as Duracell employees, as well as WEM through consulting activities.

References

- Dong W, Shi J L, Wang T S, et al. 3D zinc on carbon fiber composite framework anode for aqueous Zn-MnO₂ batteries. RSC Advances, 2018, 8(34): 19157–19163
- Chen X, Zhou Z, Karahan H E, et al. Recent advances in materials and design of electrochemically rechargeable zinc–air batteries. Small, 2018, 14(44): 1801929
- 3. Prentice G, Chang Y, Shan X. A model for the passivation of the zinc electrode in alkaline electrolyte. Journal of the Electrochemical Society, 1991, 138(4): 890–894
- 4. Parker J F, Ko J S, Rolison D R, et al. Translating materials-level performance into device-relevant metrics for zinc-based batteries. Joule, 2018, 2(12): 2519–2527
- Desai D, Wei X, Steingart D A, et al. Electrodeposition of preferentially oriented zinc for flow-assisted alkaline batteries. Journal of Power Sources, 2014, 256: 145–152
- Chao D, Zhu C R, Song M, et al. A high-rate and stable quasisolid-state zinc-ion battery with novel 2D layered zinc orthovanadate array. Advanced Materials, 2018, 30(32): 1803181
- Mao Z, White R E. Mathematical modeling of a primary zinc/air battery. Journal of the Electrochemical Society, 1992, 139(4): 1105–1113
- Cachet C, Saidani B, Wiart R. The behavior of zinc electrode in alkaline electrolytes: II. A kinetic analysis of anodic dissolution. Journal of the Electrochemical Society, 1992, 139(3): 644–654
- 9. Faegh E, Ng B, Hayman D, et al. Design of highly reversible zinc anodes for aqueous batteries using preferentially oriented electrolytic zinc. Batteries & Supercaps, 2020, 3(11): 1220–1232
- Huang S, Wu W, Su Y, et al. Insight into the corrosion behaviour and degradation mechanism of pure zinc in simulated body fluid. Corrosion Science, 2021, 178: 109071
- 11. Levy A V, Chik P. The effects of erodent composition and shape on the erosion of steel. Wear, 1983, 89(2): 151–162
- Sun K E K, Hoang T K A, Doan T N L, et al. Suppression of dendrite formation and corrosion on zinc anode of secondary aqueous batteries. ACS Applied Materials & Interfaces, 2017, 9(11): 9681–9687
- 13. He P, Huang J. Detrimental effects of surface imperfections and unpolished edges on the cycling stability of a zinc foil anode. ACS Energy Letters, 2021, 6(5): 1990–1995
- Ariosa D, Elhordoy F, Dalchiele E A, et al. Texture vs morphology in ZnO nano-rods: On the X-ray diffraction characterization of electrochemically grown samples. Journal of Applied Physics, 2011, 110(12): 124901
- 15. Michlik T, Rosin A, Gerdes T, et al. Improved discharge capacity of zinc particles by applying bismuth-doped silica coating for zinc-based batteries. Batteries, 2019, 5(1): 32
- 16. He P, Huang J. Chemical passivation stabilizes Zn anode.

- Advanced Materials, 2022, 34(18): 2109872
- 17. Faegh E, Omasta T, Hull M, et al. Understanding the synamics of primary Zn–MnO₂ alkaline battery gassing with operando visualization and pressure cells. Journal of the Electrochemical Society, 2018, 165(11): A2528–A2535
- Faegh E, Shrestha S, Zhao X, et al. In-depth structural understanding of zinc oxide addition to alkaline electrolytes to protect aluminum against corrosion and gassing. Journal of Applied Electrochemistry, 2019, 49(9): 895–907
- Faegh E, Ng B, Lenhart B, et al. Partial deployment of Al in Zn–MnO₂ alkaline battery anodes to improve the capacity and reversibility. Journal of Power Sources, 2021, 506: 230167
- Huot J Y, Malservisi M. High-rate capability of zinc anodes in alkaline primary cells. Journal of Power Sources, 2001, 96(1): 133–139
- 21. Glaeser W, Künzel-Keune S, Merkel P. The influence of discharge time on post-partial discharge gassing of zinc powder. Journal of Power Sources, 1999, 80(1–2): 72–77
- 22. Zhang X G. Fibrous zinc anodes for high power batteries. Journal of Power Sources, 2006, 163(1): 591–597
- Zhang Q, Luan J, Fu L, et al. The three-dimensional dendrite-free zinc anode on a copper mesh with a zinc-oriented polyacrylamide electrolyte additive. Angewandte Chemie, 2019, 131(44): 15988–15994
- Li H, Zhang W, Elezzabi A Y. Transparent zinc-mesh electrodes for solar-charging electrochromic windows. Advanced Materials, 2020, 32(43): 2003574
- Chamoun M, Hertzberg B J, Gupta T, et al. Hyper-dendritic nanoporous zinc foam anodes. NPG Asia Materials, 2015, 7(4): e178
- Ko J S, Geltmacher A B, Hopkins B J, et al. Robust 3D Zn sponges enable high-power, energy-dense alkaline batteries. ACS Applied Energy Materials, 2019, 2(1): 212–216
- 27. Dillip G R, Nagajyothi P C, Ramaraghavulu R, et al. Synthesis of crystalline zinc hydroxystannate and its thermally driven amorphization and recrystallization into zinc orthostannate and their phase-dependent cytotoxicity evaluation. Materials Chemistry and Physics, 2020, 248: 122946
- 28. Zhou J, Xie M, Wu F, et al. Encapsulation of metallic Zn in a hybrid MXene/graphene aerogel as a stable Zn anode for foldable Zn-ion batteries. Advanced Materials, 2022, 34(1): 2106897
- 29. Yang H, Yang Z, Wen X, et al. The *in-situ* growth of zincaluminum layered double hydroxides on graphene and its application as anode active materials for Zn–Ni secondary battery. Electrochimica Acta, 2017, 252: 507–515
- 30. Ruan P, et al. Achieving highly proton-resistant Zn–Pb anode through low hydrogen affinity and strong bonding for long-life electrolytic Zn//MnO $_2$ battery. Advanced Materials, 2023, 35(31): e2300577
- 31. Yi R, Shi X, Tang Y, et al. Carboxymethyl chitosan-modified

- zinc anode for high-performance zinc-iodine battery with narrow operating voltage. Small Structures, 2023, 4: 2300020
- 32. Chen X, Shi X, Ruan P, et al. Construction of an artificial interfacial layer with porous structure toward stable zinc-metal anodes. Small Science, 2023, 3(6): 2300007
- Bayazitoglu Y, Brotzen F R, Zhang Y. Metal vapor condensation in a converging nozzle. Nanostructured Materials, 1996, 7(7): 789–803
- 34. Yang C C, Lin S J. Improvement of high-rate capability of alkaline Zn–MnO₂ battery. Journal of Power Sources, 2002, 112(1): 174–183
- Marinković Z V, Mančić L, Marić R, et al. Preparation of nanostructured Zn–Cr–O spinel powders by ultrasonic spray pyrolysis. Journal of the European Ceramic Society, 2001, 21(10–11): 2051–2055
- Lesz S, Tański T, Hrapkowicz B, et al. Characterisation of Mg–Zn–Ca–Y powders manufactured by mechanical milling. Journal of Achievements in Materials and Manufacturing Engineering, 2020, 103(2): 49–59
- Inoguchi M, Suzuki K, Kageyama K, et al. Monodispersed and well-crystallized zinc oxide nanoparticles fabricated by microemulsion method. Journal of the American Ceramic Society, 2008, 91(12): 3850–3855
- 38. Rusu M, Sofian N, Rusu D. Mechanical and thermal properties of zinc powder filled high density polyethylene composites. Polymer Testing, 2001, 20(4): 409–417
- Beji Z, Sun M, Smiri L S, et al. Polyol synthesis of nonstoichiometric Mn–Zn ferrite nanocrystals: Structural/microstructural characterization and catalytic application. RSC Advances, 2015, 5(80): 65010–65022
- Wang C C. Method for making irregular shaped single crystal particles and the use thereof in anodes for electrochemical cells. US patent 4487651, 1984
- Lenhart B, Zuraw M, Mustain W. A scaleable method for enhancing the crystallinity of Zn powder to reduce corrosion and boost achievable capacity. Journal of the Electrochemical Society, 2023, 170(7): 070501
- 42. Bockelmann M, Becker M, Reining L, et al. Passivation of zinc anodes in alkaline electrolyte: Part I. Determination of the starting point of passive film formation. Journal of the Electrochemical Society, 2018, 165(13): A3048–A3055
- Ye L, Lai Z, Liu J, et al. Effect of Ag particle size on electrical conductivity of isotropically conductive adhesives. IEEE Transactions on Electronics Packaging Manufacturing, 1999, 22(4): 299–302
- Bockelmann M, Reining L, Kunz U, et al. Electrochemical characterization and mathematical modeling of zinc passivation in alkaline solutions: A review. Electrochimica Acta, 2017, 237: 276–298